Divergence of laser-driven relativistic electron beams

A. Debayle,[1] J. J. Honrubia,[1] E. d'Humières,[2] and V. T. Tikhonchuk[2]
[1]*ETSI Aeronáuticos, Universidad Politécnica de Madrid, Madrid, Spain*
[2]*Centre Laser Intenses et Applications, Université Bordeaux 1–CNRS–CEA, Talence, France*
(Received 17 March 2010; published 21 September 2010)

Electron acceleration by ultrahigh intensity lasers is studied by means of two-dimensional planar particle-in-cell simulations. It is shown that the full divergence of the fast electron beam is defined by two complementary physical effects: the regular radial beam deviation depending on the electron radial position and the angular dispersion. If the scale length of the preplasma surrounding the solid target is sufficiently low, the radial deviation is determined by the transverse component of the laser ponderomotive force. The random angular dispersion is due to the small scale magnetic fields excited near the critical density due to the collisionless Weibel instability. When a preplasma is present, the radial beam deviation increases due to the electron acceleration in larger volumes and can become comparable to the local angular dispersion. This effect has been neglected so far in most of the fast electron transport calculations, overestimating significantly the beam collimation by resistive magnetic fields. Simulations with a two-dimensional cylindrically-symmetric hybrid code accounting for the electron radial velocity demonstrate a substantially reduced strength and a shorter penetration of the azimuthal magnetic field in solid targets.

DOI: 10.1103/PhysRevE.82.036405 PACS number(s): 52.38.Kd, 41.75.Jv, 52.65.Ww

I. INTRODUCTION

The advent of the chirped pulse amplification technique [1] has led to a significant increase of laser energies and intensities, allowing acceleration of electrons to relativistic energies. The characteristics of laser-driven electron beams have been extensively studied in numerous experiments carried out over more than a decade [2–16]. One of the applications of those beams is the fast ignition of inertial fusion targets, in which the mean electron energy has to be relatively low, $\lesssim 1-2$ MeV, the experimental measurements are taken indirectly and their interpretation relies on numerical simulations. Full kinetic simulations of realistic time and space scales of fast electron generation and transport cannot be afforded with the present computing capability. A more simple way to study fast electron transport in dense matter is to use hybrid codes with a prescribed electron source [17–22]. The electron distribution function at the source is characterized by a few parameters such as the mean electron kinetic energy, the energy spread and the angular distribution. Beam divergence is one of the most critical parameters. Experiments show relatively small divergences that increases with the laser intensity from $\theta \sim 20°$ to 40° [half-width at half maximum (HWHM)]. Also, the measured electron beam radius is generally several times larger than the laser focal spot size [9,13–15]. One should make a difference between the macroscopic beam divergence or effective propagation angle and the microscopic angular spread of the electron distribution function in the laser-plasma interaction region [14,16]. The conservation of electron momentum in the target plane provides that, for a normal laser incidence, the electron ejection angle θ is related to its energy [23,24]: $\theta = \tan^{-1}\sqrt{2/(\gamma-1)}$, where γ is the electron Lorentz factor. This so-called ponderomotive scaling of the dispersion angle is used as a boundary condition in many transport codes that reproduced successfully some experiments at relatively low laser intensities [9,14,16,25]. However, since the mean electron energy increases with laser intensity, the ponderomotive scaling predicts a decrease of the beam divergence with intensity that is not observed neither experimentally nor in PIC simulations [15]. Moreover, this scaling does not account for the reflected laser wave. This can be a suitable approximation for short laser pulses propagating in underdense preplasmas, but the reflected laser wave may be important for solid targets [26]. Here, electrons are mainly accelerated near the critical density in a standing laser wave coupled with the induced longitudinal electric field [27–30]. Small scale inhomogeneities in the target plane could contribute also to the beam divergence. To demonstrate this effect, Adam *et al.* [31] have considered scattering of accelerated electrons by a magnetic field randomly generated in a thin layer just behind the absorption region due to the collisionless Weibel instability.

Neither the random scattering by magnetic fields nor the ponderomotive dispersion is sufficient to explain the macroscopic beam divergence. Indeed, the random scattering angle characterizes the local angular spread of the electron distribution function in the laser plasma interaction region. As the laser intensity varies within the focal spot, in a position different from the spot center, the electrons will have a mean velocity component perpendicular to the laser propagation axis. That means that the electron local mean propagation angle θ_r depends on the radial position within the laser plasma interaction region. It represents the second component of the full electron divergence that is neglected in the present fast electron transport codes [17–20,22]. This local mean propagation angle or transverse beam velocity can modify substantially the self-generated resistive magnetic field that collimates the fast electron beam. The effect of transverse beam velocity on fast electron transport is studied in this paper.

The article is organized as follows. We begin by showing that in the case of a high laser pulse contrast, without preplasma, the regular component of the fast electron beam

transverse velocity is related to the transverse component of the laser ponderomotive force and can be controlled by the laser radial profile. In this case, the beam transverse velocity is small compared to the dispersion angle, which is defined by the stochastic magnetic fields due to collisionless Weibel instability [31]. This dispersion angle is sufficient to characterize the fast electron source divergence as in Ref. [16]. We will show that in this case the self-generated resistive magnetic field near the source region strongly contributes to the beam collimation. When preplasma is included, we found that the beam divergence strongly increases due to two effects. First, the Weibel instability develops in a lower density plasma, that enhances the intensity of scattering magnetic fields and their spatial size leading to larger deviations of fast electrons. Second, the relativistic displacement of the critical density surface and the broadening of the scattering magnetic fields lead to a significant increase of the regular component of the fast electron beam. We show that this enhancement of both components of the beam divergence decreases significantly the generation of the resistive magnetic fields and deteriorates its transport. This fact must be taken into account in fast electron transport simulations of experiments with a strong prepulse [9,10,32].

II. PARAMETERS OF NUMERICAL SIMULATIONS

Collisionless two-dimensional (2D) particle-in-cell (PIC) simulations were performed with the code PICLS [33] for a p-polarized laser pulse propagating along the positive z direction and interacting at normal incidence with a 30 μm thick gold planar foil. The ionization level of ions is fixed, $Z=40$, and the electron density in the target is $80n_c$ where $n_c=4\pi^2 m_e/\mu_0 e^2\lambda_0^2$ is the electron critical density and $\lambda_0=1$ μm is the laser wavelength. The cell width is $dx=dz=\lambda_0/56$ with 40 electrons and 1 ion per cell, the simulation box size $x\times z$ is $40\times 50\lambda_0^2$, and the dense plasma is placed at $z=20\lambda_0$. The plasma has a length of 30 μm, leaving enough space to avoid any overestimated return current [34]. Absorbing boundary conditions were used for fields and particles. Particles arriving at boundaries are reflected with a thermal velocity.

The laser pulse has a maximum intensity of $I_0=5\times 10^{19}$ W cm^{-2}, a HWHM Gaussian pulse length of $\tau_0=62.5$ fs, and a HWHM radius of 6 μm. The local angular distribution function of accelerated electrons was extracted 1 μm behind the laser interaction region, just after the zone where the Weibel instability is excited, see Fig. 1. Only the electrons with energy higher than 255 keV were considered. The *local* electron distribution has been characterized by a Gaussian function,

$$f_l(\theta)=\frac{A}{\lambda_0}\exp\left[-\frac{(\theta-\theta_r)^2}{\Delta\theta_0^2}\right], \tag{1}$$

with $\theta=\tan^{-1}[p_x/p_z]$, A a constant, and with two parameters extracted from the simulations: the local electron mean propagation angle, $\theta_r(x)$, and the local dispersion angle, $\Delta\theta_0(x)$. The local dispersion angle can be related to the transverse electron temperature, while the local electron propagation angle is related to the beam transverse velocity. Both parameters were averaged over the laser pulse length.

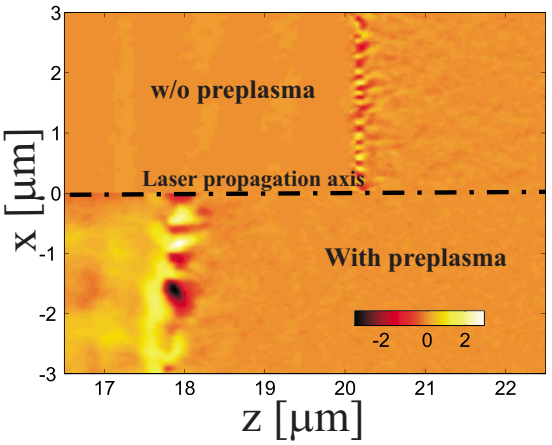

FIG. 1. (Color online) Spatial distribution of the magnetic field $eB_y\lambda_0/2\pi cm_e$ at the time of when the laser maximum intensity arrives at the left boundary of the simulation box. Top panel corresponds to the case without preplasma and bottom panel corresponds to the case with preplasma.

III. FAST ELECTRON BEAM DIVERGENCE INDUCED BY LASER INTERACTION WITH SOLID FOILS

A. Characterization of the electron angular spread

Let us discuss first the laser interaction with a solid foil without preplasma. Figure 2(a) shows the dependence of the fast electron local mean propagation angle, θ_r, on the position of electron ejection in the transverse direction. The electrons at the beam center, $x\sim 0$ μm, have zero transverse velocity ($\theta_r=0$), while the electrons sited in the beam wings propagate outwards the axis, i.e., $\theta_r>0$ for $x>0$ and $\theta_r<0$ for $x<0$. The black squares represent the propagation angle for the simulation with a transverse Gaussian shape of the laser beam. It is evident that the electron perpendicular velocity is due to the transverse component of the laser ponderomotive force. At normal incidence, $\mathbf{j}\wedge\mathbf{B}$ heating [27] is dominant and electrons oscillate near the critical density under the action of the laser Lorentz force and the longitudinal electric field. The ponderomotive force acting on electrons is [24]

$$F_x=-m_e c^2 d_x\langle a_x^2\rangle/2\gamma,$$

where $\gamma=[1+\tilde{p}_z^2+\tilde{p}_x^2+\langle a_x^2\rangle]^{1/2}$ is the electron gamma-factor averaged over the laser period, $a_x=eA_x/m_e c$ is the normalized laser transverse vector potential, A_x the laser transverse vector potential and, $\tilde{p}_x$ and $\tilde{p}_z$ the transverse and longitudinal electron momentum normalized to $m_e c$. Thus, the mean electron transverse momentum increases with time and reaches the value of $\tilde{p}_x\sim d_x\langle a_x^2\rangle\lambda_0/2\gamma$. The mean propagation angle is then

$$\theta_r=\tan^{-1}[p_x/p_z]\approx\arctan\left[\lambda_0\frac{d_x\langle a_x^2\rangle}{2\langle a_x^2\rangle}\right], \tag{2}$$

which is consistent with the longitudinal dependence of the electron deviation, $\theta_r\sim\tan^{-1}[x\lambda_0/r_0^2]$, observed in the simu-

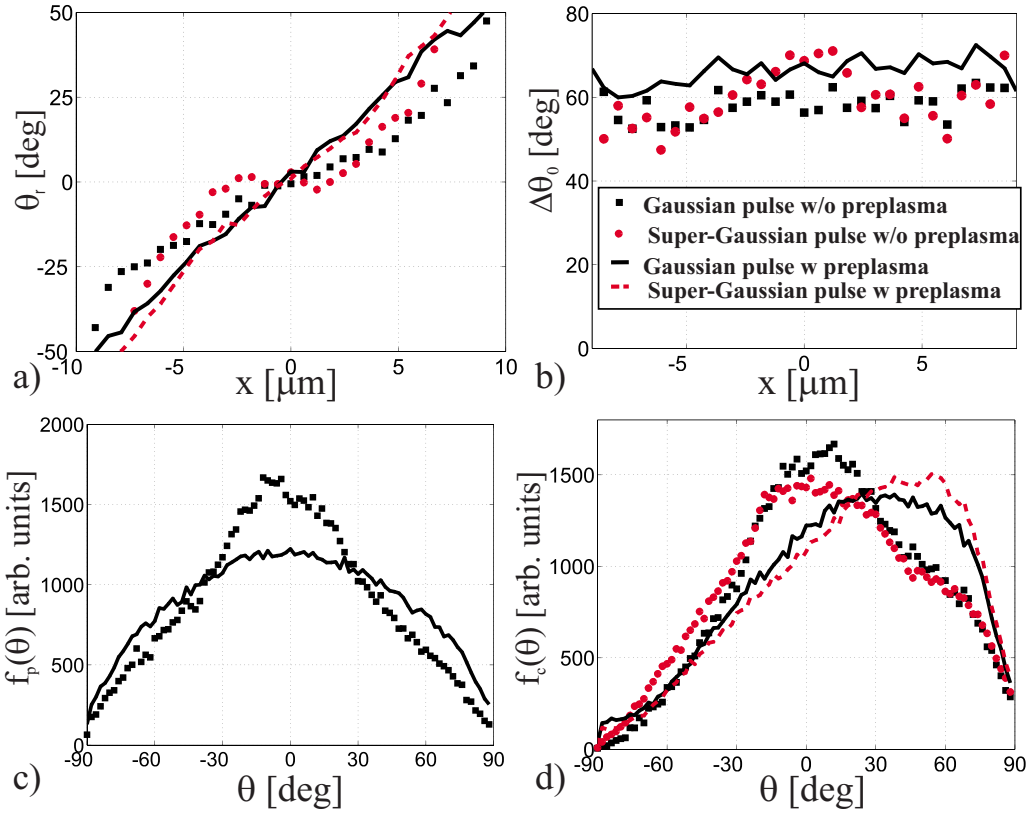

FIG. 2. (Color online) (a) Local mean electron propagation angle θ_r as a function of the transverse coordinate x. (b) Local dispersion angle $\Delta\theta_0$ versus the transverse coordinate x. (c) 2D full electron angular distribution function defined according to Eq. (5). (d) "Cylindrical" full electron angular distribution function defined by Eq. (20). Legend is shown in (b).

lation with a transverse Gaussian laser pulse with the $1/e$ radius r_0.

The mean deviation angle from the propagation axis due to the ponderomotive force is found by integration of the fast electron density distribution n_b in the transverse direction,

$$\langle\theta_r\rangle_{\text{pond}} = \int_{-\infty}^{\infty} n_b(x)|\theta_r|dx \Big/ \int n_b(x)dx, \tag{3}$$

which is $\sim 15°$ in this example. This transverse deviation can be controlled by the laser intensity profile. The result of a simulation with a transverse super-Gaussian laser beam of fourth order, $a_x^2 = a_0^2 \exp[-x^8/r_0^8]$, is shown by circles in Fig. 2(a). The deviation angle in this case is smaller, as it scales with the ponderomotive force as $\theta_r \approx \tan^{-1}[4x^7\lambda_0/r_0^8]$. Correspondingly, the electron beam mean divergence decreases to $\sim 9°$, that is about 6° less than that obtained with a Gaussian pulse.

Electron scattering in small scale magnetic fields generated near the critical density [31] due to the Weibel instability also contributes to the beam divergence. In this case, the electron mean transverse velocity is zero, but its mean square is not. In Fig. 2(b), we show the dependence of the electron dispersion angle on the transverse coordinate with the same notations as for the deviation angle in panel (a). The dispersion angle apparently depends rather weakly on the laser beam transverse profile and on the laser intensity. Its value is of the order of $\Delta\theta_0 \sim 60°$. It is larger for the super-Gaussian laser pulse with the same maximum intensity, $\Delta\theta_0 \sim 64° - 65°$. This result can be explained by the fact that the mean intensity is higher for the super-Gaussian laser pulse, that increases the electron dispersion angle according to Refs. [15,31].

In order to apply the results of our 2D PIC simulations of electron acceleration as a source for 3D axially symmetric electron transport calculations, we define the average electron angular distribution function $f_c(\theta)$ as follows:

$$f_c(\theta) = \int_0^{\infty} f_l(\theta,x)dx + \int_{-\infty}^{0} f_l(-\theta,x)dx. \tag{4}$$

Such a definition is different from the standard definition

$$f_p(\theta) = \int_{-\infty}^{\infty} f_l(\theta,x)dx, \tag{5}$$

used in 2D *planar* simulations as we want to conserve the information on the beam transverse velocity. With our definition of the full electron angular distribution function, all electrons propagating outwards the laser axis have a positive angle, $\theta > 0$.

The combined effect of transverse velocity and dispersion angle is shown in Fig. 2(d) for the electron distribution function defined by Eq. (4). The difference between the Gaussian

and super-Gaussian laser intensity distributions is small as the mean propagation angle $\langle\theta_r\rangle_{\mathrm{pond}}$ is small compared to the mean dispersion angle. Both distributions are centered at $\theta \simeq 0°$, especially the distribution obtained with the super-Gaussian laser pulse. For comparison, we present the 2D angular distribution function f_p defined by Eq. (5) in Fig. 2(c), in the case of Gaussian laser pulse without preplasma (black square symbols). The difference between the definitions (4) and (5) of the angular distribution function is small because the mean deviation angle is much smaller than the electron dispersion angle. Such an angular distribution function corresponds to the boundary condition used in many electron transport simulations [17–20,22].

B. Effect of the electron divergence angle on magnetic field generation

The ballistic propagation of a fast electron beam and its consequences on the magnetic field generation can be analyzed in a 3D cylindrically symmetric geometry assuming the electron distribution function at the injection surface as

$$f_{e1} = f(\gamma)\exp[-r^2/r_0^2 - \theta^2/\Delta\theta_0^2], \tag{6}$$

where $\theta=\tan^{-1}(p_\rho/p_z)$ is the propagation angle and $f(\gamma)$ the electron energy spectrum. The extension of the angular divergence obtained in 2D planar PIC simulations to the 3D geometry can be justified by as follows. First, the electron dispersion induced by the Weibel instability acts in both transverse directions in a similar way [31]. Second, the ponderomotive force that induces the transverse electron velocity acts also in both transverse directions as it is proportional to the gradient of the laser intensity [24].

The electron beam ballistic evolution is described by the stationary kinetic equation,

$$v_\rho \cos(\varphi-\psi)\partial_r f_e + (v_\rho/r)\sin(\varphi-\psi)\partial_\varphi f_e + v_z\partial_z f_e = 0, \tag{7}$$

where $\varphi=\widehat{(x\mathbf{e_x},\mathbf{r})}$ and $\psi=\widehat{(\mathbf{p_x},\mathbf{p}_\rho)}$ are the azimuthal angles in the real space and the momentum space, respectively. The geometry of electron motion is shown in Fig. 4(a) in Appendix A. The solution of Eq. (7) can be written as $f_e(r,z,p_\rho,p_z)=f_{e1}(R,p_\rho,p_z)$, where

$$R = \sqrt{[r\cos(\varphi-\psi) - p_\rho z/p_z]^2 + r^2\sin^2(\varphi-\psi)}, \tag{8}$$

and the function f_{e1} is defined by the boundary condition (6) at $z=0$. As demonstrated in Appendix A, in the limit of small dispersion angle, $\Delta\theta_0 \ll 1$, and near the interaction region $z=0$, the evolution of the mean beam radius can be written as

$$\langle r\rangle = \frac{2}{\sqrt{\pi}}\frac{\int\int r^2 f_e dr d\mathbf{p}}{\int\int r f_e dr d\mathbf{p}} \sim r_0(1+z^2/z_0^2), \tag{9}$$

with $z_0=r_0 g_1/\Delta\theta_0$, and g_1 is a factor of the order of unity that depends on the electron energy spectrum. According to this solution, a beam without initial transverse velocity propagates parallel to the laser axis and preserves its radius along the "collimation" length $z_0 \sim r_0/\Delta\theta_0$. It diverges strongly at distances $z > z_0$. This fact corroborates with the local propagation angle θ_r, that is defined as

$$\theta_r = \frac{\int d\mathbf{p}(p_\rho/p_z)\cos[\varphi-\psi]f_e}{\int d\mathbf{p} f_e} = \frac{rz}{r_0 z_0}\Delta\theta_0, \tag{10}$$

see also Appendix A. The parabolic behavior, Eq. (9), is valid near the laser-plasma interaction region. Far away from it, $z \gg z_0$, the beam divergence becomes linear, $\langle r\rangle \approx \Delta\theta_0 z$. These results and the geometric interpretation of the beam ballistic propagation are presented in Appendix A.

A relatively long beam collimation length facilitates generation of the resistive magnetic field. This effect can be qualitatively estimated with a rigid beam model [35]. The magnetic field $\mathbf{B}$ and the plasma electron temperature T_e are estimated with a set of simplified field equations,

$$\nabla\wedge\mathbf{E} = -\partial_t\mathbf{B}, \quad \mathbf{j}_b = -\mathbf{j}_e = -\sigma\mathbf{E}, \tag{11}$$

coupled to the plasma electron energy equation,

$$\frac{3}{2}n_e\partial_t T_e = \mathbf{j}_b\cdot\mathbf{E}. \tag{12}$$

Here, we assume that the beam current $\mathbf{j}_b$ is neutralized by the return current $\mathbf{j}_e$, the Spitzer electric conductivity, $\sigma \sim \sigma_0(T_e/T_0)^{3/2}$, is defined by the electron ion collisions with $\sigma_0=3\varepsilon_0^2(2\pi T_0)^{3/2}/Ze^2\sqrt{m_e}\ln[2\pi T_0/\hbar\omega_{pe}]$, where $\omega_{pe}^2 = e^2 n_e/m_e\varepsilon_0$ is the plasma frequency, T_0 is the initial plasma temperature, and the plasma ionization level is Z. In the assumption of weak divergence, the plasma electron heating and the magnetic field generation are mainly due to the current longitudinal component $j_{bz}=-e\int v_z f_e d\mathbf{p} \approx -en_b(r,z)c$. Knowing the evolution of the mean beam radius according to Eq. (9), the beam density can be written as

$$n_b(r,z,t) \approx n_{b0}\frac{r_0^2}{\langle r\rangle^2}\exp\left[-\frac{r^2}{\langle r\rangle^2}\right], \tag{13}$$

and the solution to Eqs. (11) and (12) reads

$$T_e = T_0\left(\frac{5}{2}\frac{\zeta}{\tau_T}+1\right)^{2/5}H[\zeta], \tag{14}$$

$$B_\theta = \frac{3n_e r T_0}{j_{bz}\langle r\rangle^2}\left(1-\frac{(1+\zeta/2\tau_T)}{(5\zeta/2\tau_T+1)^{3/5}}\right)H[\zeta] \tag{15}$$

with the Heaviside function $H(x)$, the local characteristic heating rate $\tau_T(r,z)=3\sigma_0 n_e/2j_{bz}(r,z)^2$, and the beam head position $\zeta=t-z/c$. The magnetic field, given by Eq. (15), is presented in Fig. 3(b). It has been compared with the results obtained with the hybrid code [32] describing the propagation of the electron beam in 3D axially symmetric geometry. The magnetic field obtained with the hybrid code is shown in

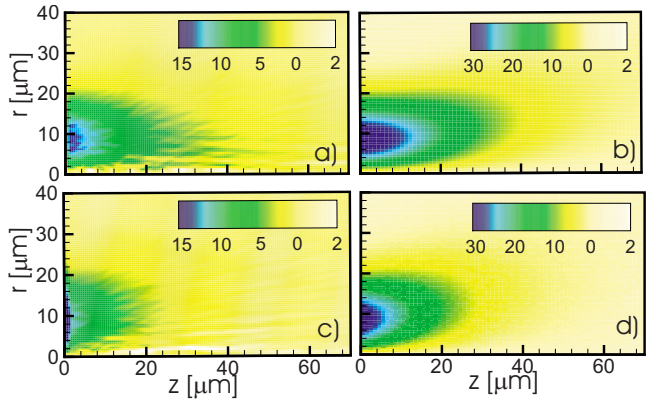

FIG. 3. (Color online) (a) Azimuthal magnetic field B_θ in T, at time $t=700$ fs, obtained with the hybrid code for the electron beam injected without transverse velocity in a plasma of gold (collisions of fast electrons are neglected). The beam maximum density $n_{b0}=1.2\times10^{19}$ cm^{-3}, the beam energy is 1 MeV, and the dispersion angle $\Delta\theta_0=30°$. (b) Azimuthal magnetic field B_θ in T according to formula Eq. (15) for the same parameters than in panel (a). (c) Same figure as in panel (a) for an electron beam injected with the mean propagation angle $\langle\theta_r\rangle=10°$ and the dispersion angle $\Delta\theta_0=20°$. (d) Azimuthal magnetic field B_θ in T according to formula Eq. (15) with the radius defined by Eq. (21) for an electron beam injected with the mean propagation angle $\langle\theta_r\rangle=10°$ and the dispersion angle $\Delta\theta_0=20°$.

Fig. 3(a) assuming a source of monoenergetic electrons of 1 MeV with the angular distribution function given by Eq. (6). The dispersion angle is set to of $\Delta\theta_0=30°$, which is smaller than the one found in the PIC simulations shown in Fig. 2(b) in order to enhance the "collimation" effect due to the beam injection. The initial beam density, $n_{b0}\sim10^{19}$ cm^{-3}, is such that the generated magnetic field does not have a significant effect on the electron penetration length.

The magnetic fields shown in panels (a) and (b) are very similar although amplitude is weaker in the hybrid simulation as the beam density varies as a Gaussian function in time. This similarity demonstrates that the magnetic field generation is correlated with the beam ballistic propagation and thus depends strongly on the electron source characteristics. The transverse position, r_m, of the peak magnetic field, B_m, evolves as

$$r_m(z,t)=\frac{\langle r\rangle}{\sqrt{2}}\ln^{1/2}\left[6\frac{\zeta}{\tau_T(0,z)}\right],$$

and the peak magnetic field reads

$$B_m(z,t)\approx\frac{3\sqrt{3}n_eT_0}{8j_{bz0}\langle r\rangle}\sqrt{\frac{\zeta}{\tau_{T0}}}\ln\left[\frac{\zeta r_0^4}{6\tau_{T0}\langle r\rangle^4}\right], \qquad (16)$$

where $j_{bz0}=j_{bz}(0,0)$ and $\tau_{T0}=\tau_T(0,0)$. The magnetic field penetration length, L_{B1}, can be estimated with the condition $B_m(L_{B1},t)/B_m(0,t)\simeq1/2$. At later times, $t\gg L_{B1}/c$, the characteristic magnetic field depth, $L_{B1}=z_0\ln^{1/4}[t/6\tau_{T0}]$, is of the order of the beam collimation length. That is, the magnetic field generation is just a consequence of a collimated electron injection. The larger the beam radius r_0 or the smaller the dispersion angle, the longer the beam penetration depth. This result is consistent with other simulations [17,19,22,36], where one can see this characteristic beam collimation due to the parallel beam injection. However, such a description of the local electron angular distribution function with one parameter, the dispersion angle, is valid only for high contrast laser pulses, where the preplasma scale length L is much smaller than the laser beam radius r_0.

IV. FAST ELECTRON BEAM DIVERGENCE INDUCED BY LASER INTERACTION OF SOLID FOILS WITH PRE-PLASMA

A. Characterization of the electron angular spread

Ultra high intensity laser beams often present a prepulse with a duration of a few ns, which is sufficiently intense to generate a plasma in the target front side with characteristic length comparable or even larger than the laser spot radius. In this configuration, our PIC simulations of electron acceleration show that the preplasma has a strong effect on the beam divergence for two reasons. First, electrons are accelerated in a larger volume around the critical density and the critical layer is pushed forward by the laser longitudinal ponderomotive force and by the relativistically induced transparency. Thus, the laser-plasma interaction region cannot be considered as a planar surface. This effect "ballistically" increases the electron transverse velocity behind interaction region. Second, although the energy of accelerated electrons is higher in the case with preplasma, the magnetic fields generated by the Weibel instability are stronger and with a larger scale because the mean background electron density is lower (see the bottom panel of Fig. 1). These fields enhance the fast electron scattering.

An exponential preplasma profile with a characteristic length of $L_n=1$ μm has been considered in the simulations. The critical layer is sited at a distance of ~4 μm from the maximum plasma density at $z=20$ μm. In Fig. 2(a), the dependence of the local electron mean propagation angle on the transverse coordinate x is plotted by the black solid line and the red dashed line for the Gaussian and super-Gaussian laser intensity profiles, respectively. In both cases the transverse velocity is higher than in simulations without preplasma and there is no significant dependence on the laser radial shape. This is due to the small effects of the transverse ponderomotive force and the nonuniform relativistically induced transparency. As already discussed for the case without preplasma, the effect of the transverse ponderomotive force is small as the laser focal spot is large compared to the laser wavelength. A small effect induced by bending of the relativistic critical density surface can be explained by a strong density gradient. Indeed, with the exponential preplasma density profile, $n_e=n_{\max}\exp[-z/L_n]$, the depth of the critical density modulation, $L_n\ln[1+a_0^2]\sim2$ μm, is small compared to the beam radius, $r_0\sim6$ μm. For a larger gradient plasma scale length comparable with the laser beam radius, the critical surface bending can induce an electron beam transverse deviation comparable with the dispersion angle induced by the Weibel instability.

Under the simulation conditions assumed in this Section, the major contribution to the electron transverse velocity comes from: (i) a higher acceleration length, (ii) a larger coupling between the Weibel instability magnetic fields and the laser evanescent wave, of the order of the laser wavelength. Without preplasma, all electrons are accelerated approximately at the same place and suffer the scattering during a very short length, $\sim\lambda_0\sqrt{n_c/n_e}$. With preplasma, the electrons are accelerated in a volume that depends on the plasma density gradient at the laser absorption position, sited between the critical density n_c and $n_c\sqrt{1+a_x^2}$. In this region of underdense plasma, electrons are already scattered by the nonhomogeneous self-generated magnetostatic fields that can be seen in bottom panel of Fig. 1. Then, in the underdense plasma, the electrons are scattered by the Weibel instability generated magnetic fields coupled with the laser evanescent wave during a length of the order of $\sim\lambda_0$. Assuming that electron scattering occurs during a length L, and that electrons may enter in the acceleration zone at different depths with an equal probability, the local propagation angle, $\theta_{r,\mathrm{bal}}$, after the interaction region is a superposition of the local propagation angles of all electrons, that is,

$$\theta_{r,\mathrm{bal}} \approx \frac{1}{L}\int_0^L dz'\,\theta_r(z-z'), \tag{17}$$

where θ_r is defined by Eq. (10). Note that we can directly generalize the mean propagation angle to 3D cylindrical geometry as the Weibel instability, responsible of electron scattering, does not depend on the laser polarization direction. Then the expression for the local mean propagation angle reads

$$\theta_{r,\mathrm{bal}}(z\sim L) \sim \frac{rL}{2r_0^2}\Delta\theta_0^2. \tag{18}$$

This rough estimate shows that a small preplasma length is sufficient for increasing of the transverse velocity as the intrinsic dispersion angle of electrons is large as can be seen in Fig. 2(b). The total electron deviation angle after the interaction region can be represented as a sum of contributions of the transverse ponderomotive force Eq. (2) and the "ballistic" effect Eq. (18),

$$\theta_r(r) \approx \arctan\left[\frac{rL}{2r_0^2}\Delta\theta_0^2 + \lambda_0\frac{d_r\langle a_r^2\rangle}{\langle a_r^2\rangle}\right]. \tag{19}$$

Figure 2(b) shows the dependence of the dispersion angle on the transverse coordinate for simulations with preplasma. The values of the dispersion angle are comparable to those obtained in the simulations without preplasma. This is due to the contribution of two opposite effects. First, the dispersion angle generated by the electron oscillations in laser field and the electron scattering in Weibel-generated magnetic field are higher than those found in the case without preplasma since the mean background electron density in the acceleration zone is much lower [31]. Second, the dispersion angle decreases due to electron acceleration from a volume. Indeed, while the transverse velocity increases with the laser plasma interaction depth, the dispersion angle decreases. The full divergence angle f_p, defined by Eq. (5), is depicted in Fig. 2(c) by black line for the Gaussian laser pulse. This distribution function, which is not relevant for cylindrical geometries, gives however an indication on the initial mean dispersion angle because it is an invariant of the ballistic beam propagation. The mean dispersion angle is much larger than in the simulations without preplasma, however, this value, $\Delta\theta_0\sim 70°$, is overestimated as our simulations are collisionless. We expect that electron collisions and plasma ionization will decrease slightly the magnitude of magnetic fields induced by the Weibel instability responsible of electron scattering.

The "cylindrical" full angular electron distribution function, defined by the Eq. (4), accounts for both the dispersion angle and the mean propagation angle, as shown in Fig. 2(d). Unlike the simulations without preplasma, the mean angular deviation angle is of the order of 25° for both Gaussian and super-Gaussian laser pulses. The electron beam is already divergent after the interaction region because the length of the interaction region, $L\sim 2-3$ μm, is comparable with the "collimation" length $z_0\sim r_0\sim 6$ μm, giving a mean propagation angle, according to Eqs. (2) and (18), $\langle\theta_r\rangle=\langle\theta_r\rangle_{\mathrm{pond}}+\langle\theta_r\rangle_{\mathrm{bal}}\sim 25°$. Such an angular distribution function is more appropriate for interpretation of experimental results where the laser prepulse intensity is sufficiently high to generate a preplasma of a size comparable with the laser beam radius.

B. Magnetic field generation by divergent electron beams

Propagation of a radially divergent electron beam has been simulated with the hybrid code described in [32]. The angular distribution function of the injected beam was represented as

$$f_l = f(\gamma)\exp\left[-\frac{r^2}{r_0^2}-\frac{(\chi-\theta_r)^2}{\Delta\theta_0}\right], \tag{20}$$

where $\chi=\tan^{-1}[p_\rho\cos(\varphi-\psi)/p_z]$ is the electron momentum angle with respect to the local ejection axis defined by the angle θ_r given by Eq. (19). All electrons have the same energy of 1 MeV. The generalization of the angular distribution function from planar geometry (1) to cylindrical geometry Eq. (20), is discussed in Appendix B. Figure 3(c) shows the map of magnetic field obtained with this angular distribution function. Although the sum of the deviation angle, $\langle\theta_r\rangle=10°$, and the dispersion angle, $\Delta\theta_0=20°$, is the same as the dispersion angle in the case without preplasma ($\Delta\theta_0=30°$), the beam diverges more strongly. The magnetic field penetration depth decreases as well as its strength. The reduction of the magnetic field penetration can be estimated by assuming that $\langle\theta_r\rangle\ll\Delta\theta_0\ll 1$. By solving the ballistic kinetic Eq. (7) with the boundary condition (20), one can show that near the laser-plasma interaction region $z\sim 0$, the beam radius evolves as

$$\langle r\rangle = g_2\langle\theta_r\rangle z + r_0\left(1+\frac{z^2}{z_0^2}\right), \tag{21}$$

where g_2 is a factor around unity that depends on the fast electron spectrum $f(\gamma)$. The details of calculation are pre-

sented in Appendix C. In this case, the beam diverges from the very beginning and its radius, in the ballistic approximation, increases linearly with the propagation distance. Far away from laser-plasma interaction region, the radius evolution becomes linear, $\langle r\rangle \approx (\langle \theta_r\rangle + \Delta\theta_0)z$.

Figure 3(d) shows the magnetic field obtained from the analytical solution for the angular dependence of the electron distribution function Eq. (15) and the electron beam radius Eq. (21). The similarity with the numerical solution obtained with a hybrid code is evident. This confirms the validity of the ballistic approximation. The magnetic field penetration depth, L_{B2}, is smaller than that obtained for the case without preplasma because of the stronger beam divergence. Using the same approach than that employed to estimate L_{B1}, the magnetic field penetration length can be written as

$$L_{B2} \sim L_{B1}(1 - \langle \theta_r\rangle/\Delta\theta_0),$$

with $g_1 \sim g_2 \sim 1$. The second term represents a decrease of several tens of percent, which has a dramatic effect on the fast electron transport.

V. CONCLUSION

We have shown by means of 2D PIC simulations, that the angular divergence of electron beam generated in relativistic laser plasma interactions has two different components. First, the angular dispersion is due to the fast electron scattering in the stochastic magnetic fields generated by the Weibel instability and coupled to the laser field [31]. The dispersion angle is thus enhanced for stronger laser intensity or lower background electron density. The second component is the electron deviation in transverse direction due to the laser transverse ponderomotive force and propagation effects in preplasma. For short laser pulses or high density plasmas, where the laser hole boring [27] is negligible, the initial transverse beam velocity weakly depends on the laser transverse intensity gradient, but depends strongly on the preplasma scale length and on the dispersion angle. This divergence component must be taken into account in order to avoid strong overestimations of self-generated fields and their effects on electron transport. The transverse beam velocity suppresses the resistive magnetic fields generated in plasma and undermines the beam collimation. The control of Weibel instability in the laser-plasma interaction region is one of the key issues for reducing electron scattering. It can be achieved by lowering the laser intensity or by increasing the plasma electron density and plasma collisionality.

In closing, we would like to point out the important consequences of the beam collimation decrease for the fast ignition of inertial fusion targets [5,37]. Since the transport codes used to compute the electron energy deposition in the compressed core do not resolve the laser-plasma interaction region, it is typically assumed an initial distribution function for fast electrons that does not include the net radial velocity of the beam at injection [38–41]. As we have shown in this paper, both angular dispersion and radial velocity have to be included in hybrid codes to reproduce the features of fast electron transport. If, as in most of the simulations performed so far, only the angular dispersion is taken into account, the magnetic collimation of the fast electron beam can be overestimated and thus the laser energies required to ignite a target can be underestimated. This effect will be quantified in future publications.

ACKNOWLEDGMENTS

This work has been partially supported by the HiPER project and the research Grant No. ENE2009-11668 from the Spanish Ministry of Education and Research. Calculations have been performed at the CESVIMA, CINES, and CCRT supercomputing centers.

APPENDIX A: BEAM BALLISTIC PROPAGATION WITHOUT INITIAL TRANSVERSE VELOCITY

The beam ballistic propagation with the boundary condition given by Eq. (6) can be estimated near the laser plasma interaction region $z \ll z_0$. The distribution function $f_{e1}(R, p_\rho, p_z)$, with the radius R defined by Eq. (8), can be expanded near $z \sim 0$,

$$f_e = f_{e1} + \frac{\partial f_{e1}}{\partial R|_r}\frac{dR}{dz|_0}z + \frac{1}{2}\left[\frac{\partial^2 f_{e1}}{\partial R|_r^2}\left(\frac{dR}{dz|_0}\right)^2 + \frac{\partial f_{e1}}{\partial R|_r}\frac{d^2R}{dz|_0^2}\right]z^2. \tag{A1}$$

In the small angle approximation, $\Delta\theta_0 \ll 1$, we find

$$f_e = f_{e1}(r, p_\rho, p_z)\left[1 + 2\frac{rz}{r_0^2}\frac{p_\rho}{p_z}\cos[\varphi - \psi] + \frac{z^2}{r_0^2}\left(\frac{2r^2}{r_0^2}\cos^2[\varphi - \psi] - 1\right)\frac{p_\rho^2}{p_z^2}\right]. \tag{A2}$$

Then, we calculate the mean radius defined by Eq. (9), with the integration limits $\int_0^\infty r dr \int_0^{2\pi} d\psi \int_0^\infty p_\rho dp_\rho \int_{p_{\min}}^\infty dp_z$ and where $p_{\min} > 0$ since we are interested in electrons propagating forward. After some algebra, one finds

$$\langle r\rangle = r_0\left(1 + \frac{z^2}{r_0^2}g_1\Delta\theta_0^2\right), \tag{A3}$$

where

$$g_1\Delta\theta_0^2 \approx \frac{\int_0^\infty \int_{p_{\min}}^\infty (p_\rho^2/p_z^2) f(\gamma)\exp[-\theta^2/\Delta\theta_0^2] p_\rho dp_\rho dp_z}{\int_0^\infty \int_{p_{\min}}^\infty f(\gamma)\exp[-\theta^2/\Delta\theta_0^2] p_\rho dp_\rho dp_z}. \tag{A4}$$

The local propagation angle near the laser-plasma interaction region can be estimated using the distribution function expansion of Eq. (A2). The local propagation angle is defined by

$$\theta_r = \frac{\int_0^{2\pi} d\psi \int_0^{\infty} p_\rho dp_\rho \int_{p_{\min}}^{\infty} dp_z \frac{p_\rho}{p_z} \cos[\varphi - \psi] f_e}{\int_0^{2\pi} d\psi \int_0^{\infty} p_\rho dp_\rho \int_{p_{\min}}^{\infty} dp_z \frac{p_\rho}{p_z} f_e}. \quad \text{(A5)}$$

Taking into account the expression of f_e of Eq. (A2), and keeping only the first order term in z, one has

$$\theta_r = \frac{rzg_1 \Delta\theta_0^2}{r_0^2}. \quad \text{(A6)}$$

The parabolic approximation, Eq. (A3), is valid for $z \ll z_0$. Far from the laser-plasma interaction region, the beam radius becomes a linear function of z. Indeed, the beam radius, defined by Eq. (9), can be estimated as follows. First, the beam density, defined by $n_b = \int_0^{2\pi} d\psi \int_0^{\infty} p_\rho dp_\rho \int_{p_{\min}}^{\infty} dp_z f_{e1}(R, p_\rho, p_z)$, can be calculated with the substitution: $p_\rho/p_z = \tan\theta$ and $\gamma = \sqrt{\tilde{p}_\rho^2 + \tilde{p}_z^2 + 1}$. One finds

$$n_b = 2\pi \int_0^{\infty} \exp\left[-\frac{r^2 + z^2 \tan^2\theta}{r_0^2} - \frac{\theta^2}{\Delta\theta_0^2} \right] I_0\left[2\frac{rz}{r_0^2} \tan\theta \right] \tan\theta \sqrt{1 + \tan^2\theta}\, d(\tan\theta) \int_{\gamma_{\min}}^{\infty} \frac{\gamma^2 - 1}{\gamma} f(\gamma) d\gamma, \quad \text{(A7)}$$

where we have used $\int_0^{2\pi} \exp(a\cos[x])dx = 2\pi I_0[a]$, with $I_0[x]$ the 0-order modified Bessel function I [42]. Then, in the approximation $r \gg r_0$ and $z \gg z_0$, and introducing $n_{b0} = \sqrt{\pi} \int_{\gamma_{\min}}^{\infty} f(\gamma) \sqrt{\gamma^2 - 1}/\gamma d\gamma$, we have

$$n_b = n_{b0} \frac{r_0}{z} \sqrt{1 + \frac{r^2}{z^2}} \exp\left[-\left(\frac{\tan^{-1}[r/z]}{\Delta\theta_0} \right)^2 \right]. \quad \text{(A8)}$$

Finally, for small angle $\Delta\theta_0 \ll 1$, one has

$$\langle r \rangle \approx \Delta\theta_0 z. \quad \text{(A9)}$$

The beam ballistic propagation without radial velocity, as defined by Eq. (9), can be understood geometrically with the scheme in Fig. 4(b). If all electrons start to propagate with the characteristic dispersion angle $\Delta\theta_0$, the beam radius divergence is "visible" when the electrons propagating from the laser/interaction region center ($r=0$, $z=0$) with the propagation angle $\theta = \Delta\theta_0$, cross the trajectory of electrons propagating from the position $r = r_0$ with angle $\theta = 0°$. There trajectories are represented by the black dotted line in Fig. 4(b). Thus, the beam divergence becomes visible after the characteristic depth, $z_0 \sim r_0/\tan[\Delta\theta_0]$.

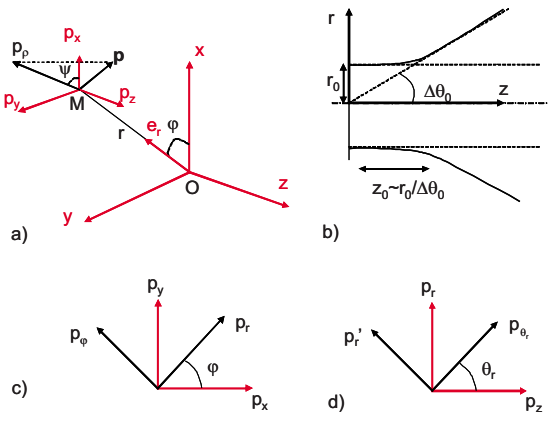

FIG. 4. (Color online) (a) Cylindrical symmetry geometry in the real space (r, φ, z) and in the momentum space (p_ρ, ψ, p_z) used in the present article. (b) Scheme of the beam ballistic propagation without initial transverse velocity. (c) Momentum reference frame (p_r, p_φ, p_z) derived from the cylindrical coordinate (r, φ, z). (d) Momentum reference frame $(p_r', p_\varphi, p_{\theta_r})$ defined by a rotation of angle θ_r of the momentum reference frame (p_r, p_φ, p_z).

APPENDIX B: ANGULAR DISTRIBUTION FUNCTION IN CYLINDRICAL SYMMETRY

According to the 2D planar simulations, the electron local angular distribution function can be approximated by Eq. (1). Here we generalize this angular distribution function to the 3D cylindrical geometry presented in Fig. 4(a). Electrons in a small volume around the position $(r, \varphi, 0)$ in cylindrical coordinates, have propagation angles normally distributed around the angle θ_r with the characteristic dispersion angle $\Delta\theta_0$. The local propagation angle θ_r, shown in Fig. 4(d), is in the plane (e_r, z) due to the cylindrical symmetry of the laser beam. We present in Figs. 4(a), 4(c), and 4(d), the coordinate systems used to express Eq. (20). The momentum reference frame (p_r, p_φ, p_z) is derived from the spatial cylindrical coordinate (r, φ, z). $(p_r', p_\varphi, p_{\theta_r})$ is the momentum reference frame defined by a rotation of angle θ_r of reference system (p_r, p_φ, p_z) around the axis p_φ. In this latter momentum reference frame, electrons are propagating in the direction p_{θ_r} with the dispersion angle $\Delta\theta_0$. Therefore, the angular electron distribution function is written as

$$f_l = \exp\left[-\left(\frac{\tan^{-1}[\sqrt{(p_r'^2 + p_\varphi^2)/p_{\theta_r}^2}]}{\Delta\theta_0} \right)^2 \right]. \quad \text{(B1)}$$

To simplify the formulation of the beam radius ballistic evolution, we neglect the component p_φ^2. This is equivalent to assume that electrons in the plane $(p_\varphi, p_{\theta_r})$ have equal probability to have an angle between $-90°$ and $90°$. This assumption does not affect the ballistic evolution of the beam as we are in cylindrical geometry. Taking into account that p_r'

$=p_r \cos\theta_r - p_z \sin\theta_r$ and $p_{\theta_r}=p_z \cos\theta_r + p_r \sin\theta_r$, one finds

$$f_l = \exp\left[-\left(\frac{\tan^{-1}[p_r/p_z]-\theta_r}{\Delta\theta_0}\right)^2\right]. \quad \text{(B2)}$$

Finally, in the cylindrical momentum reference frame (p_ρ, ψ, p_z), defined by $p_x=p_\rho \cos\psi$ and $p_y=p_\rho \sin\psi$, it comes

$$f_l = \exp\left[-\left(\frac{\chi-\theta_r}{\Delta\theta_0}\right)^2\right], \quad \text{(B3)}$$

with $\chi=\tan^{-1}[p_\rho \cos(\varphi-\psi)/p_z]$.

APPENDIX C: BEAM BALLISTIC PROPAGATION WITH INITIAL TRANSVERSE VELOCITY

The ballistic propagation with an initial transverse velocity can be studied similarly to the case without transverse velocity presented in Appendix A. The kinetic equation Eq. (7) has two characteristics,

$$R = \sqrt{[r\cos(\varphi-\psi) - p_\rho z/p_z]^2 + r^2 \sin^2(\varphi-\psi)}, \quad \text{(C1)}$$

$$\cos[\varphi-\psi] = -\frac{p_z}{p_\rho}\frac{dR}{dz}. \quad \text{(C2)}$$

Using the boundary condition (20) and assuming that $\theta_r \ll \Delta\theta_0$, the first order expansion of the distribution function at $z\sim 0$ reads

$$f_e = f_{e2}(r,p_\rho,p_z)\left[1 + \frac{2rz}{r_0^2}\frac{p_\rho}{p_z}\cos[\varphi-\psi] + \frac{2z}{r}\frac{p_\rho^3/p_z^3}{\Delta\theta_0^2}\sin^3[\varphi-\psi]\cos[\varphi-\psi]\right]. \quad \text{(C3)}$$

Taking into account that $\int_0^{2\pi}\sin^3 x \cos x \exp[-(\cos x - a)^2]dx=0$, one can calculate the dependence of the beam radius on the propagation distance as

$$\langle r\rangle = r_0\left(1 + g_2\langle\theta_r\rangle\frac{z}{r_0} + \frac{z^2}{z_0^2}\right), \quad \text{(C4)}$$

where

$$g_2\langle\theta_r\rangle = \frac{4}{\sqrt{\pi}}\frac{\int_0^{2\pi}\int_0^{\infty}\int_{p_{\min}}^{\infty}\cos[\varphi-\psi]\frac{p_\rho}{p_z}f_{e2}(r,p_\rho,p_z)p_\rho dp_\rho dp_z d\psi}{\int_0^{2\pi}\int_0^{\infty}\int_{p_{\min}}^{\infty} f_{e2}(r,p_\rho,p_z)p_\rho dp_\rho dp_z d\psi}. \quad \text{(C5)}$$

In the approximation $\theta_r \ll \Delta\theta_0$, the second order term, $z_0 = r_0/g_1\Delta\theta_0$, is the same as in Eq. (A3).

[1] D. Strickland and G. Mourou, Opt. Commun. **56**, 219 (1985).
[2] K. B. Wharton, S. P. Hatchett, S. C. Wilks, M. H. Key, J. D. Moody, V. Yanovsky, A. A. Offenberger, B. A. Hammel, M. D. Perry, and C. Joshi, Phys. Rev. Lett. **81**, 822 (1998).
[3] M. H. Key *et al.*, Phys. Plasmas **5**, 1966 (1998).
[4] F. Pisani *et al.*, Phys. Rev. E **62**, R5927 (2000).
[5] R. Kodama *et al.*, Nature (London) **412**, 798 (2001).
[6] M. Zepf *et al.*, Phys. Plasmas **8**, 2323 (2001).
[7] J. J. Santos, F. Amiranoff, S. D. Baton, L. Gremillet, M. Koenig, E. Martinolli, M. Rabec Le Gloahec, C. Rousseaux, D. Batani, A. Bernardinello, G. Greison, and T. Hall, Phys. Rev. Lett. **89**, 025001 (2002).
[8] R. Kodama *et al.*, Nature (London) **432**, 1005 (2004).
[9] R. B. Stephens *et al.*, Phys. Rev. E **69**, 066414 (2004).
[10] E. Martinolli, M. Koenig, F. Amiranoff, S. D. Baton, L. Gremillet, J. J. Santos, T. A. Hall, M. Rabec-Le-Gloahec, C. Rousseaux, and D. Batani, Phys. Rev. E **70**, 055402(R) (2004).
[11] P. A. Norreys, J. S. Green, J. R. Davies, M. Tatarakis, E. L. Clark, F. N. Beg, A. E. Dangor, K. L. Lancaster, M. S. Wei, M. Zepf, and K. Krushelnick, Plasma Phys. Controlled Fusion **48**, L11 (2006).
[12] E. Martinolli *et al.*, Phys. Rev. E **73**, 046402 (2006).
[13] K. L. Lancaster *et al.*, Phys. Rev. Lett. **98**, 125002 (2007).
[14] J. J. Santos, A. Debayle, P. Nicolaï, V. Tikhonchuk, M. Manclossi, D. Batani, A. Guemnie-Tafo, J. Faure, V. Malka, and J. J. Honrubia, Phys. Plasmas **14**, 103107 (2007).
[15] J. S. Green *et al.*, Phys. Rev. Lett. **100**, 015003 (2008).
[16] M. Storm, A. A. Solodov, J. F. Myatt, D. D. Meyerhofer, C. Stoeckl, C. Mileham, R. Betti, P. M. Nilson, T. C. Sangster, W. Theobald, and C. Guo, Phys. Rev. Lett. **102**, 235004 (2009).
[17] J. R. Davies, A. R. Bell, M. G. Haines, and S. M. Guérin, Phys. Rev. E **56**, 7193 (1997).
[18] L. Gremillet, G. Bonnaud, and F. Amiranoff, Phys. Plasmas **9**, 941 (2002).
[19] J. J. Honrubia, A. Antonicci, and D. Moreno, Laser Part. Beams **22**, 129 (2004).
[20] D. R. Welch, D. V. Rose, M. E. Cuneo, R. B. Campbell, and T. A. Mehlhorn, Phys. Plasmas **13**, 063105 (2006).
[21] T. Yokota, V. Nakao, T. Johzaki, and K. Mima, Phys. Plasmas **13**, 022702 (2006).
[22] A. P. L. Robinson, M. Sherlock, and P. A. Norreys, Phys. Rev. Lett. **100**, 025002 (2008).
[23] C. I. Moore, J. P. Knauer, and D. D. Meyerhofer, Phys. Rev. Lett. **74**, 2439 (1995).
[24] B. Quesnel and P. Mora, Phys. Rev. E **58**, 3719 (1998).
[25] J. J. Honrubia, C. Alfonsín, L. Alonso, B. Pérez, and J. A. Cerrada, Las. Part. Beams **24**, 217 (2006).
[26] W. Yu, V. Bychenkov, Y. Sentoku, M. Y. Yu, Z. M. Sheng, and K. Mima, Phys. Rev. Lett. **85**, 570 (2000).
[27] S. C. Wilks, W. L. Kruer, M. Tabak, and A. B. Langdon, Phys. Rev. Lett. **69**, 1383 (1992).

[28] W. Yu, M. Y. Yu, Z. M. Sheng, and J. Zhang, Phys. Rev. E **58**, 2456 (1998).
[29] D. Bauer and P. Mulser, Phys. Plasmas **14**, 023301 (2007).
[30] R. Mishra, Y. Sentoku, and A. J. Kemp, Phys. Plasmas **16**, 112704 (2009).
[31] J. C. Adam, A. Héron, and G. Laval, Phys. Rev. Lett. **97**, 205006 (2006).
[32] J. J. Honrubia, M. Kaluza, J. Schreiber, G. D. Tsakiris, and J. Meyer-ter vehn, Phys. Plasmas **12**, 052708 (2005).
[33] Y. Sentoku and A. J. Kemp, J. Comput. Phys. **227**, 6846 (2008).
[34] J. Tonge, J. May, W. B. Mori, F. Fiuza, S. F. Martins, R. A. Fonseca, L. O. Silva, and C. Ren, Phys. Plasmas **16**, 056311 (2009).
[35] J. R. Davies, Phys. Rev. E **65**, 026407 (2002).
[36] J. Fuchs *et al.*, Phys. Rev. Lett. **91**, 255002 (2003).
[37] M. Tabak, J. Hammer, M. E. Glinsky, W. L. Kruer, S. C. Wilks, J. Woodworth, E. M. Campbell, M. D. Perry, and R. J. Mason, Phys. Plasmas **1**, 1626 (1994).
[38] S. Atzeni, A. Schiavi, J. J. Honrubia, X. Ribeyre, G. Schurtz, P. Nicolaï, M. Olazabal-Loumé, C. Bellei, R. G. Evans, and J. R. Davies, Phys. Plasmas **15**, 056311 (2008).
[39] A. A. Solodov and R. Betti, Phys. Plasmas **15**, 042707 (2008).
[40] J. J. Honrubia and J. Meyer-ter-Vehn, Plasma Phys. Controlled Fusion **51**, 014008 (2009).
[41] T. Johzaki, Y. Sentoku, H. Nagatomo, H. Sakagami, Y. Nakao, and K. Mima, Plasma Phys. Controlled Fusion **51**, 014002 (2009).
[42] M. Abramowitz and I. A. Stegun, *Handbook of Mathematical Functions with Formulas, Graphs, and Mathematical Tables* (Dover, New York, 1964), 9th Dover printing, 10th GPO printing ed.